Advanced Energy Materials

ADVANCED ENERGY MATERIALS
www.advenergymat.de

RESEARCH ARTICLE

Single-Atom Catalysts with Microenvironment Tuned by High Entropy for Efficient and Stable Alkaline Hydrogen Evolution Reaction

Bangxin Li | Mingyue Yuan | Yihao Liu | Jinwen Zhang | Yuting Miao | Xuhui Xiong | Jiachen Sun | Renchao Che | Heyong He

Department of Chemistry, Laboratory of Advanced Materials, Shanghai Key Lab of Molecular Catalysis and Innovative Materials, State Key of Porous Materials For Adsorption and Conversion, State Key Laboratory of Coatings for Advanced Equipment, College of Smart Materials and Future Energy, Fudan University, Shanghai, China

Correspondence: Renchao Che (rcche@fudan.edu.cn) | Heyong He (heyonghe@fudan.edu.cn)

Received: 6 September 2025 | **Revised:** 31 October 2025 | **Accepted:** 10 November 2025

Keywords: electronic structure modulation | high stability | hydrogen evolution reaction | metal-support interaction | single-atom catalysts

ABSTRACT

Conventional non-noble hydrogen evolution reaction catalysts are plagued by excessive hydrogen adsorption and instability. To overcome this, we pioneer a high-entropy single-atom (HESA) catalyst via precise anchoring of multiple transition metals on carbon supports. The HESA catalyst achieves record-breaking alkaline HER performance of 44 mV@10 mA cm^{-2} (matching commercial Pt/C catalyst) and 300 h stability, resolving the persistent activity-stability trade-off. Systematical characterizations reveal that low-coordination metal sites induce significant metal-support charge redistribution. Electronegative supports withdraw electrons from metal centers, while π-back-donation downshifts metal d-band centers, optimizing the Gibbs free energy of intermediate H atoms (ΔG_{H^*}). Atomic-scale imaging further confirms uniform charge distribution and Ångström-level electric field response. Crucially, adjacent multi-metal sites synergistically lower energy barriers for both water dissociation and hydrogen desorption through a synergistic electronic buffering effect. This work establishes entropy-driven microenvironment engineering as a paradigm for cooperative optimization of active sites and electronic structures, opening avenues for durable non-precious catalysts.

1 | Introduction

In the context of the energy transition, hydrogen energy has emerged as one of the key solutions, playing a crucial role in achieving the carbon neutrality target [1, 2]. The electrochemical hydrogen evolution reaction (HER), as a fundamental step in water splitting, offers an eco-friendly, cost-effective, and efficient source of green hydrogen [3, 4]. It not only meets the growing energy demand but also mitigates environmental challenges by effectively converting and storing intermittent energy sources into chemical energy. Platinum (Pt) remains the most effective component for HER, enabling minimal overpotential and rapid kinetics due to its favorable hydrogen binding energy [5, 6]. The exceptional performance of Pt-based catalysts stems from their near-optimal hydrogen adsorption energy, which enables kinetically balanced adsorption and desorption of hydrogen intermediates (H) at active sites, a key factor in overcoming the rate-determining step for the HER in alkaline media [7, 8]. Nevertheless, the high cost and limited availability of Pt have spurred an urgent need to explore alternative catalyst materials. Unlike noble metals, the practical deployment of non-noble metal electrocatalysts is fundamentally constrained by their

intrinsically excessive hydrogen adsorption energy, which kinetically poisons active sites through sluggish hydrogen desorption, representing the most critical barrier beyond cost or stability concerns [9, 10].

Building on the challenge of excessive hydrogen adsorption in non-noble metals, the key to mitigating this lies in engineering their atomic configuration. Atomization, dispersing metals into single atoms anchored on tailored supports, directly addresses the strong adsorption issue [11–13]. This strategy exploits the unique low-coordination environment of isolated metal atoms, which weakens hydrogen binding energy and facilitates desorption, thereby preventing kinetic poisoning of active sites. However, these highly active single-atom sites face inherent instability. Non-noble metals often suffer from degradation under reaction conditions, while purely carbon-based supports, though stable, lack sufficient activity [14, 15]. To reconcile this activity-stability dilemma, robust encapsulation strategies become essential. By chemical confining the atomically dispersed metal centers within a protective carbon matrix, encapsulation prevents overexposure, suppresses aggregation or leaching, and crucially, fine-tunes the local electronic environment to avoid excessive activity that could trigger self-degradation [16, 17]. This synergistic combination, atomic dispersion to optimize adsorption energy, coupled with encapsulation to ensure longevity, represents a targeted approach to emulate Pt performance.

In this study, we develop a general strategy based on carbon-encapsulated active metal sites to simultaneously control catalytic activity and enhance oxidation resistance. This strategy is exemplified through the creation of carbon-encapsulated high-entropy single-atom (HESA) catalysts. We propose that the unique atomic configuration within the carbon shell, distinct from conventional metals or alloys, holds the potential to address the fundamental challenge of excessive hydrogen adsorption energy in non-noble metals. Furthermore, the carbon encapsulation design is anticipated to stabilize these highly active sites under harsh conditions, like alkaline media, for the HER. This integrated approach of confinement and atomic-level engineering aims to overcome the critical barriers of activity-stability trade-offs in non-precious HER catalysts. By demonstrating this concept, this work not only advances the development of efficient and stable catalysts but also provides a versatile platform and new perspective for designing next-generation materials for energy conversion and storage.

2 | Results

2.1 | Controlled Synthesis of HESA Catalyst with Atomic-level Dispersion

The multi-metal single-atom sites (Fe, Co, Ni, Cu, Mn) with stable and predictable coordination environments were achieved through the hydrolysis of metal acetates, followed by pyrolysis and anchoring the multi-metal atoms onto a hollow carbon framework. The high-entropy single-atom sites are constructed via two critical stabilization pathways (Figure 1a): 1) hydrolysis of coordinated hydroxyacetates [M(OH)(OAc)] (M = Fe, Co, Ni, Cu, and Mn) (Figure S1) transforms the precursors into a hydroxyl-bridged layered double hydroxide (LDH) phase (Figure S2), where the edge-sharing [$M(OH)_6$] octahedra prevents metal aggregation [18, 19], and 2) subsequent low-temperature pyrolysis (350°C) under reducing atmosphere induces the carbon matrix to anchor these metal ions as atomically dispersed sites through formation of M(N) moieties, with the pre-organized LDH structure ensuring uniform metal distribution. Scanning electron microscopy (SEM) and high-angle annular dark-field scanning transmission electron microscopy (HAADF-STEM) results confirm the hollow structure of the catalyst, exhibiting a 500 nm diameter and 30 nm wall thickness in a hollow hexadecahedral morphology (Figure 1b,c). Furthermore, energy-dispersive spectroscopy (EDS) and atomic-scale electron energy loss spectroscopy (EELS) microanalysis (Figure 1d,e) demonstrate both the random distribution of single atoms and capture the ionization edge of five kinds of atoms at atomic level, with no evidence of segregation. Additionally, focused ion beam (FIB) technology (Figure 1f) was employed to slice the structure, revealing the cross-section and confirming the hollow structure without the presence of clusters or larger-sized particles. Atomic-resolution HAADF-STEM images captured by aberration-corrected transmission electron microscopy (AC-TEM) (Figure 1g,h) reveal the presence of individual atoms. The surface of the HESA catalyst (Figure S3) demonstrates a high specific surface area (SBET = 218 m^2 g^{-1}) along with defective microchannels (diameter = 2.9 nm). The observed nanoporous structure exhibits type IV adsorption-desorption isotherms with H3 hysteresis loops, further confirming the plate-like particle stacking mechanism [20, 21].

Inductively coupled plasma-optical emission spectroscopy (ICP-OES) was used to determine the elemental composition Fe, Co, Ni, Cu, and Mn, revealing atomic ratios of 20.36 %, 19.81 %, 20.39 %, 18.71 %, and 20.73 % (Table S1). X-ray diffraction (XRD) analysis (Figure S4) shows no metallic diffraction peak, while X-ray absorption near-edge structure (XANES) data (Figure S5) reveal Fe, Co, Ni, Cu, and Mn absorption edges positioned lower than their respective metallic foil standards [22, 23]. The single atoms exist in oxidized states, with their absorption edges positioned between the metallic and oxide references, confirming the formation of chemical bonds with the support material. To unravel the atomic-scale structure of the high-entropy single-atom catalyst, pair distribution function (PDF) analysis with structural refinement was performed (Figure 1i). The dominant peaks at 0.93 and 1.78 Å for C(N) coordination, and metallic atom peaks (3.1, 5.1, and 6.9 Å) are significantly longer than the metallic bond distances (2.48 Å for Fe-Fe bond, 2.44 Å for Ni—Ni bond), demonstrating the absence of metal clustering [24]. Furthermore, the attenuated peak intensity and broadened profile beyond 0.9 Å reveal enhanced atomic disorder, which originates from the configurational entropy maximization in this high-entropy system [25].

2.2 | Enhanced Hydrogen Evolution Reaction Performance of HESA Catalyst

Due to the thermodynamic influences on coordination and aggregation state of metal atoms even the metal crystal growth, grain size is highly sensitive to temperature and heating duration [26, 27]. Controlling these factors enables the formation of metal crystal structures under the same conditions. Based on this, we synthesized a high-entropy alloy (HEA) catalyst by adjusting the

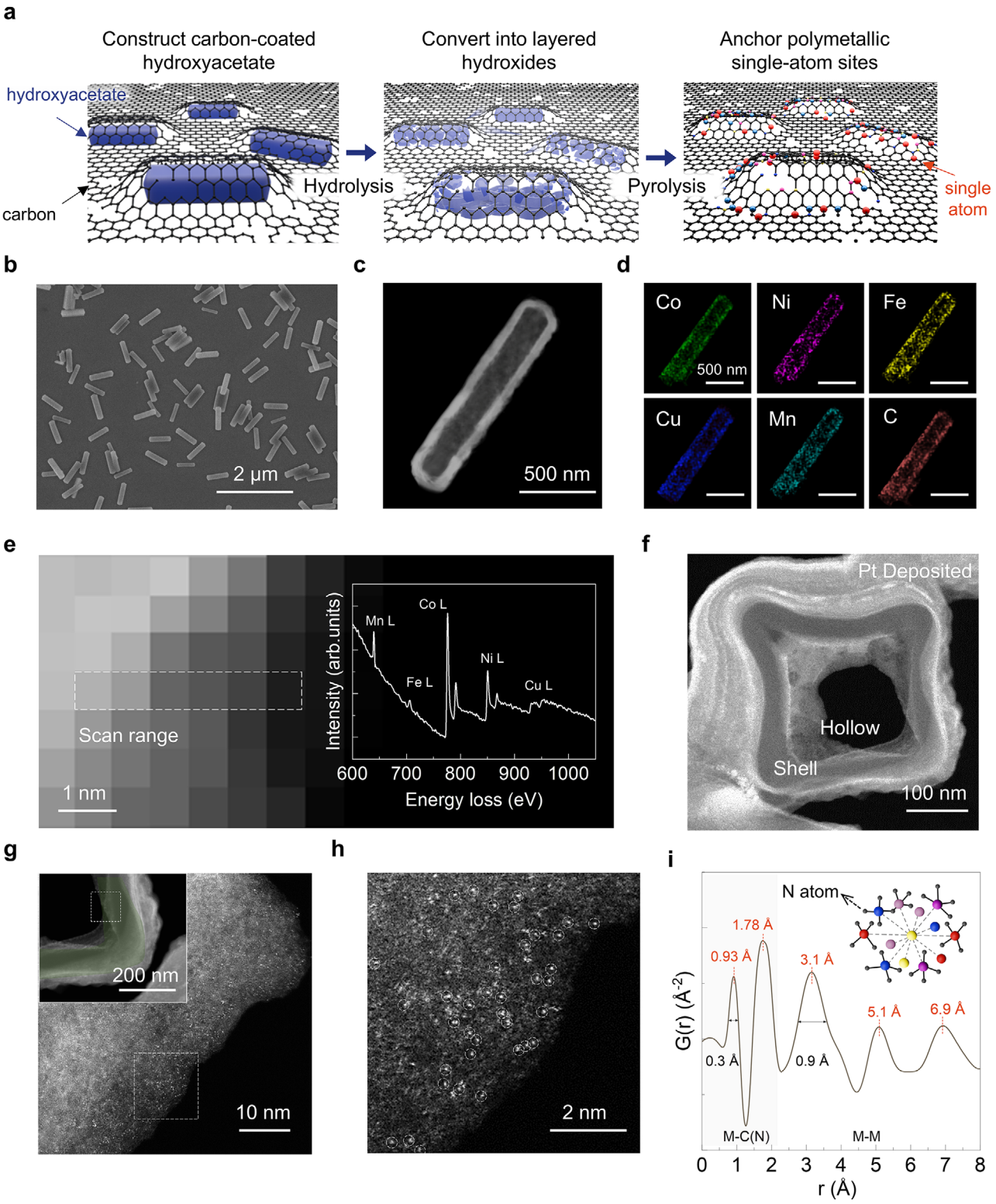

Figure 1 | Structural and elemental characterization of the synthesized multi-metallic single atom. (a) Schematic illustration of the general synthesis process, depicting the transformation of metallic acetate into multi-single atom states catalyst capping by carbon through hydrolysis and pyrolysis process. (b) Scanning electron microscopy image of the structures of synthesized HESA catalyst. (c) High-angle annular dark-field scanning transmission electron microscopy (HAADF-STEM) image of the structures of HESA catalyst. (d) Energy-dispersive X-ray spectroscopy elemental mapping of Fe, Co, Ni, Cu, Mn, and C. (e) High-resolution electron energy loss spectroscopy (EELS) results of the HESA catalyst. The insert in (e) illustrates the regions captured from the scan range and the corresponding EELS spectrum (right). (f) STEM image of the focused ion beam (FIB)-milled cross-section of the HESA catalyst. (g) HAADF-STEM image of shell region (white box in inset) showing atomic dispersion. (Inset: false-color low-magnification overview) (h) Atomic-resolution zoom of boxed area in (g) confirming metal site dispersion. (i) Pair distribution function analysis, showing characteristic bonding environments, with corresponding schematic illustrations.

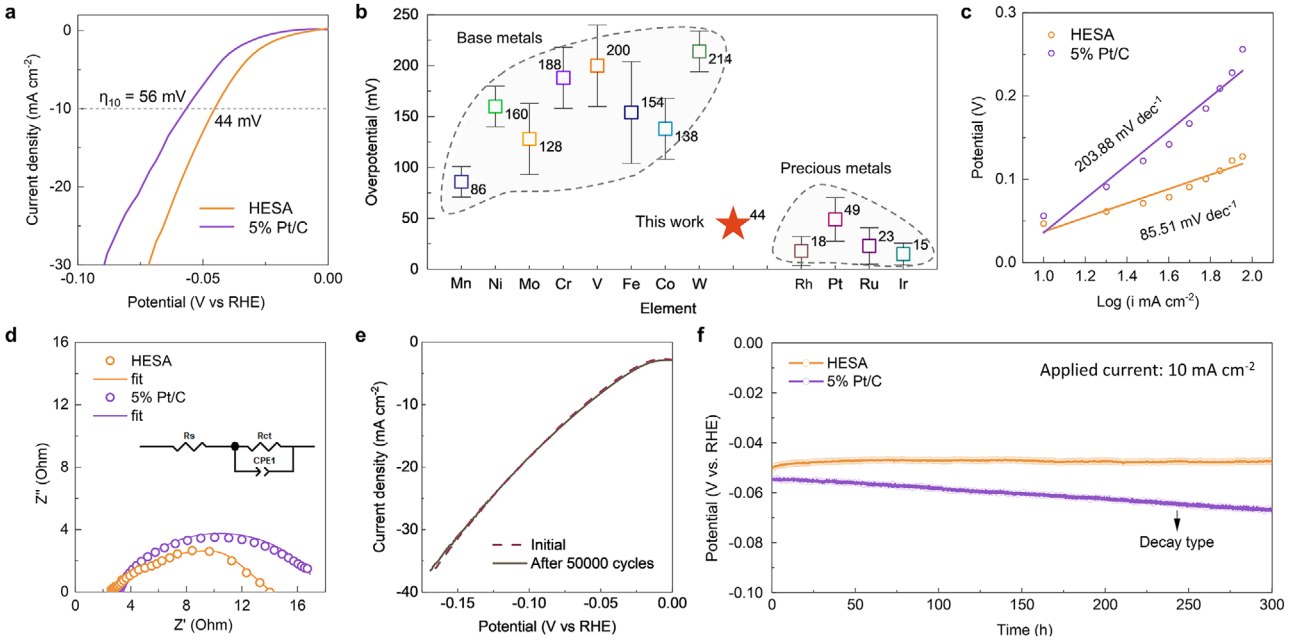

Figure 2 | Electrochemical hydrogen generation performance in alkaline conditions. (a) The iR-corrected linear sweep voltammetry (LSV) curves of HESA and 5% Pt/C catalysts in 1 M KOH solution with a scan rate of 5 mV s^{-1}. (b) Comparison of overpotential at a current density of 10 mA cm^{-2} for element-based catalysts. The data points compared in (b) are sourced from References (Supporting Information). (c) The corresponding Tafel plots of as-prepared HESA and 5% Pt/C catalysts. (d) Nyquist plots and fit data of EIS for HESA and 5% Pt/C catalysts. (e) LSV curves of HESA catalyst before and after 50 000 cyclic voltammetry cycles. (f) Chronoamperometry data recorded for HESA and 5% Pt/C catalysts at a constant current of 0.03 A.

heating temperature to 600°C (Figure S6). To evaluate the potential electrocatalytic activity of the synthesized HESA catalyst, for comparison, HEA catalyst and commercial 5% Pt/C catalyst were also tested as reference materials. Its HER performance was first measured in a 1.0 M KOH aqueous solution using a standard three-electrode configuration. All polarization curves were calibrated against a reversible hydrogen electrode (RHE). As shown in Figure 2a and Figure S7, HESA catalyst exhibits an exceptionally low overpotential (η_{10} = 44 mV), outperforming both HEA catalyst (135 mV) and 5% Pt/C catalyst (56 mV). Furthermore, Figure 2b and Table S2 compare the overpotentials of the HESA catalyst with those of reported non-noble transition and noble metal catalysts. HESA catalyst with Fe, Co, Ni, Cu and Mn achieves catalytic performance comparable to that of noble metals (Pt, Pd, Ru) through the synergistic effects of high entropy and single-atom active sites, even demonstrating lower overpotentials in some cases. HESA catalyst exhibits a Tafel slope of 85.51 mV dec^{-1}, significantly lower than that of 5% Pt/C catalyst (203.88 mV dec^{-1}) and the HEA catalyst (177.61 mV dec^{-1}) (Figure 2c). This result indicates that the introduction of high-entropy single atoms optimizes the electrochemical hydrogen adsorption or desorption process. The lower Tafel slope of the HESA catalyst compared to that of Pt/C suggests a change in the rate-determining step and potentially more favorable reaction kinetics.

The electrochemical active surface area (ECSA), a critical parameter for assessing the intrinsic catalytic activity, was determined through electrochemical double-layer capacitance (C_{dl}) measurements derived from cyclic voltammetry (CV) scans at varying sweep rates (Figure S8). The HESA catalyst exhibits the highest C_{dl} value (16.01 mF cm^{-2}), substantially exceeding those of the reference catalysts (4.55 and 3.54 mF cm^{-2} for 5% Pt/C and HEA catalyst, respectively). This pronounced enhancement in double-layer capacitance directly correlates with the unique multi-single-atom interface and engineered surface roughness of the HESA catalyst, which collectively facilitate superior exposure of electrochemically active sites for the HER [28, 29]. Subsequent normalization of the linear sweep voltammetry (LSV) data by the respective ECSA values (Figure S9) reveals the exceptional intrinsic activity of the HESA catalyst, exhibiting an outstanding overpotential of merely 99.6 mV at a normalized current density of 1 mA cm^{-2}_{ECSA}. This performance not only surpasses that of the HEA catalyst but also confirms the highest areal density of active sites in the HESA catalyst, thereby establishing a clear structure-activity relationship between the atomic-scale interfacial design and the enhanced HER performance. Meanwhile, HESA catalyst exhibits a significantly lower R_p value (12 Ω) compared to Pt/C catalyst (16 Ω) and HEA catalyst (25 Ω) catalysts according to the Nyquist plots and equivalent circuit (Figure 2d), indicating a remarkable enhancement in charge transfer capability [30].

As a critical parameter for evaluating advanced electrocatalysts, the electrochemical durability of HESA catalyst in 1.0 M KOH electrolyte was further assessed. As shown in Figure 2e, the *I–V* curve of HESA catalyst remains almost unchanged after 50 000 CV cycles. In contrast, the *I–V* curves of HEA catalyst and Pt/C catalyst (Figure S10) show significant degradation after 50 000 cycles. Additionally, the chronoamperometric curve in Figure 2f reveals that the HESA catalyst experiences no degradation after 300 h, while 5% Pt/C and HEA catalyst (Figure S11) decay lasting for 300 h, further demonstrating exceptional long-term stability of the HESA catalyst. Moreover, ICP-OES characterization before and after stability test indicates no significant changes in the

composition of HESA catalyst (Tables S3). To assess the practical applicability of the HESA catalyst, we further evaluated its performance under more technologically relevant conditions using an anion exchange membrane water electrolyzer (AEMWE). The HESA-based electrode demonstrated a superior current density of 400 mA cm^{-2} at 2.41 V and maintained excellent stability over 180 h shown in Figure S12, significantly outperforming the conventional catalyst.

2.3 | Validation of Active Site Stability and Coordination Environment in HESA Catalyst

Post-cycling AC-TEM characterization (Figure 3a) confirms that the HESA catalyst maintains its atomically dispersed state. The contrast of the metal sites remains consistent with the pristine state. Furthermore, quantitative EDS elemental mapping analysis (Figure 3b) demonstrates that the uniform distribution of the polymetallic components is preserved without disruption. In contrast, for the HEA catalyst (Figure S13 and Table S3), it is also evident that precipitation and aggregation of nanoparticles occurred after the cycling tests. X-ray photoelectron spectroscopy (XPS) analysis of the catalyst before and after the HER cycling (Figure 3c; Figures S14 and S15) reveal that the binding energy shifts for all five elements (Fe, Co, Cu, Ni, and Mn) are less than 1 eV. The small binding energy shift likely originates from physical effects, specifically an increased surface charge induced by the accumulation of oxygen-containing groups (including C—O for 286.6 eV and C═O for 288 eV) on the carbon support during cycling, as confirmed by post-test XPS analysis [31, 32]. Significantly, reversible +2/+3 valence oscillations were observed on the surfaces of the redox-active metals, facilitating the regeneration of active sites through dynamic valence cycling. Fourier transform extended X-ray absorption fine structure (FT-EXAFS) provides further insight (Figure 3d). After cycling, the peaks within the 1.2-1.5 Å range in the R-space spectra, corresponding to the first-shell coordination distance, exhibit minimal changes for all five metal centers (Fe, Co, Ni, Cu, Mn). This main peak indicates strengthened bonding between the metal centers (M) and light elements (C) in the substrate (M—C bonding). Concurrently, the M—M scattering peaks beyond 2.0 Å in the FT-EXAFS spectra completely disappeared, indicating the absence of metal-metal (M—M) scattering or features characteristic of higher coordination shells associated with ordered structures (nanoparticles or clusters) [33, 34]. This dynamically optimized structure promotes structural flexibility and enhances the electronic structure, primarily through strengthened interactions with light elements (M—C). The resulting optimized electronic structure is characterized by enhanced electron-donating capability.

We further analyzed the chemical nature of intermediates using ^{1}H magic-angle spinning nuclear magnetic resonance spectroscopy (^{1}H MAS NMR). Fresh and cycled HESA catalysts exhibit two distinct peaks at 1.3 and 4.9 ppm (Figure 3e), attributed to terminal (OH_t) and bridging (OH_b) hydroxyl species, respectively [35, 36]. The OH_b signal is significantly enhanced in the cycled HESA catalyst, indicating that bridging oxygen sites are highly effective with adsorbing generated protons. Furthermore, in situ electrochemical Raman analysis (Figure 3f) was employed to further investigate the interfacial water structure at different potentials. In the range of 3000–3800 cm^{-1}, the Raman band splits into three distinct peaks, corresponding to three types of water. The shifts of these peaks exhibit strong dependence on the electrode potential, indicating that the observed Raman signals primarily originate from the first few water layers near the surface. Previous studies have linked the peak (≈3620 cm^{-1}) to alkali ion hydrated interfacial water (H_2O-alkali). In contrast, the peaks located at ≈3420 and ≈3210 cm^{-1} are attributed to 1H-down and 2H-down interfacial water molecules, respectively [37, 38]. The H-down interfacial water molecules are likely the primary activated species on the catalyst surface. As the potential shifts toward more positive values, the relative intensity of H-down interfacial water increases significantly, suggesting that the formation of H-down interfacial water provides evidence for the generation of reactive intermediates, such as adsorbed hydrogen (*H), during the HER process in alkaline environments. This phenomenon also indicates that the HESA catalyst facilitates rapid adsorption of surface water. Additionally, the Raman shifts induced by the vibrational Stark effect as a function of potential reveal that H-down interfacial water molecules are more sensitive to the applied potential compared to H_2O-alkali in HESA catalyst, exhibiting a red-shift as the potential becomes increasingly positive. This observation further confirms that the interaction between H-down water molecules and the electrode surface is stronger than that of H_2O-alkali. It is concluded that the introduction of single-atom sites can modulate the interfacial microenvironment, including the decrease of hydrogen bonding interactions and the enrichment of interfacial water molecules.

2.4 | Unraveling the Relationship Between Electronic Structure and Catalytic Activity in HESA Catalyst

We elucidate the structural characteristics and catalytic mechanism of HESA catalysts through theoretical calculations and experimental characterizations. The variation in catalytic performance for the HER stems from the distinct electronic structure characteristics of different metal sites, which differentially regulate three key reaction steps: water molecule activation, water dissociation, and H^+ reduction. According to Figure 4a,b and Table S4, in the initial water adsorption stage, Mn (−0.33 eV), Co (−0.20 eV) and Cu (−0.15 eV) sites exhibit optimal thermodynamic spontaneity, effectively accepting water molecules while avoiding excessive adsorption. Subsequently, in the rate-determining water dissociation step, Ni (0.50 eV) and Cu (0.65 eV) sites demonstrate superior catalytic activity, where their relatively lower energy barriers originate from the effective catalysis of O—H bond cleavage, though this step remains the kinetic bottleneck of the overall reaction. Meanwhile, the migration energy for molecules from Co-site to Ni-site was rather lower than the dissociation energy (Figure S16). Although the energy differences between these steps appear minor (<0.2 eV), these variations ultimately lead to significant distinctions in catalytic efficiency through the synergistic effects of multiple active sites across different reaction stages, fully demonstrating the remarkable performance advantages of transition metal catalysts in HER.

Atomic-scale charge distribution analysis (Figure 4c) reveals a 6 Å charge perturbation radius around single-atom Fe centers, with pronounced charge redistribution at Fe-C interfaces confirming

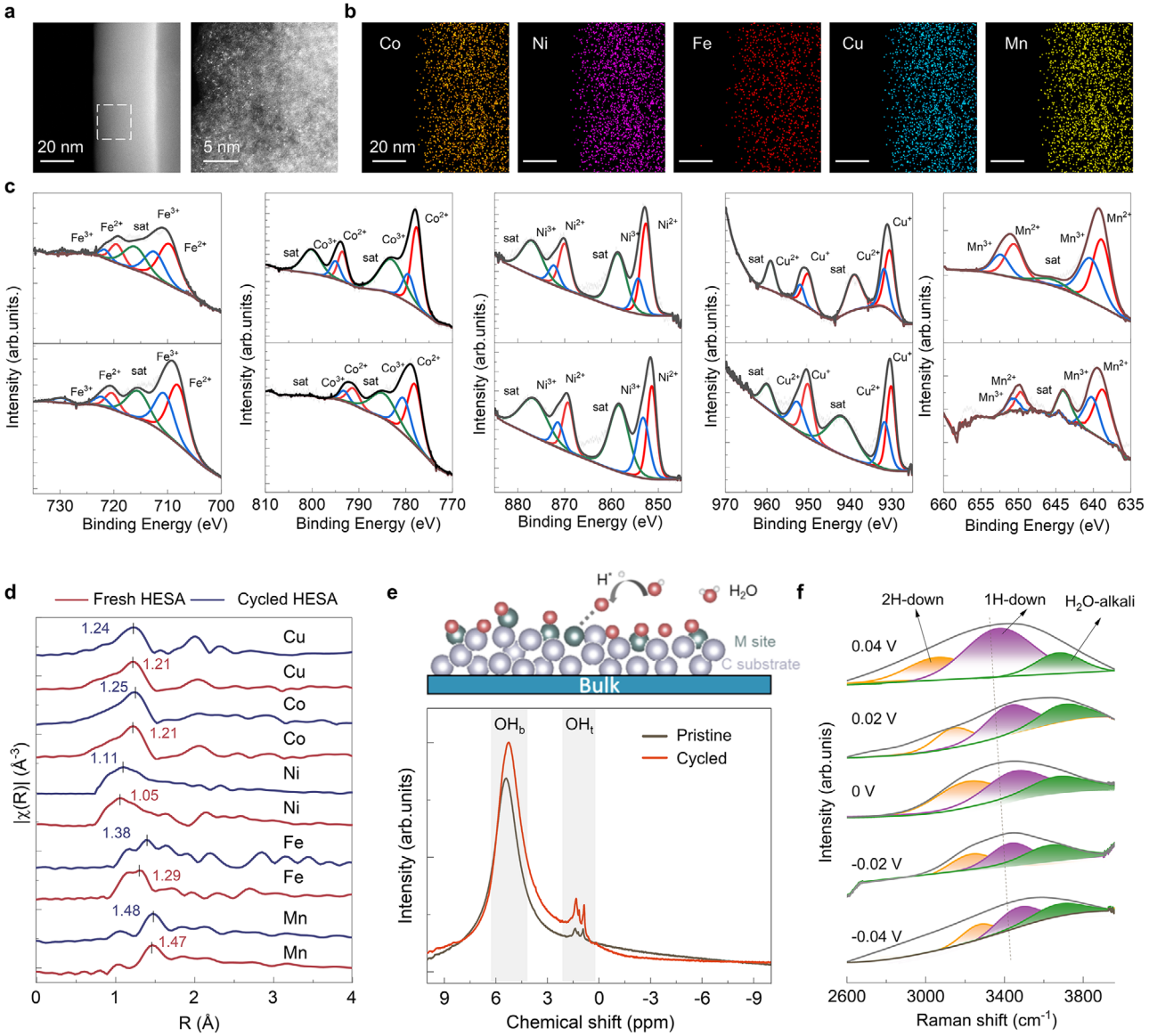

Figure 3 | Bulk and surface structure characterization of HESA catalyst. (a) High-angle annular dark-field scanning transmission electron microscopy (HAADF-STEM) image of HESA catalyst after cycling. Zoomed-in atomic-resolution HAADF-STEM image, revealing atomic-level dispersion of metal sites in the white rectangular box. (b) Energy-dispersive X-ray spectroscopy elemental mapping of Co, Ni, Fe, Cu, and Mn after cycling. (c) High-resolution X-ray photoelectron spectroscopy of Fe 2*p*, Co 2*p*, Cu 2*p*, Ni 2*p*, and Mn 2*p* for HESA catalyst before (bottom) and after (top) cycling. (d) Fourier transform extended X-ray absorption fine structure spectra of HESA catalyst before (red lines) and after (blue lines) 50 000 cycles with phase correction. (e) ^{1}H magic angle spinning nuclear magnetic resonance spectra of HESA before (black line) and after cycling (red line). Terminal hydroxyl species (OH_t) and bridging hydroxyl species (OH_b) are identified, with the corresponding structural model and hydroxyl groups on the surface established based on crystallographic data of HESA catalyst. (f) In situ Raman spectra for HESA catalyst under applied voltage from −0.04 to 0.04 V.

strong metal-support interactions [39]. Bader charge analysis identifies Fe single atoms as electron donors, forming localized positive centers, while coordinated carbon atoms serve as electron acceptors with interfacial charge accumulation. Comparable charge redistribution capabilities were observed for other metal sites (Figure S17). The static electron holography characterization via transmission electron microscopy (Figure 4d) clearly reveals the existence of high-density dipoles (positive-negative charge pairs) on the catalyst surface, which originates from the presence of high-entropy single atoms. These dipoles exhibit a remarkably uniform distribution with an inter-dipole spacing of approximately 0.3 nm (Figure 4e), demonstrating a distinct contrast to the interfacial charge accumulation typically observed in conventional nanoscale catalytic materials. This atomic-scale charge separation pattern provides direct evidence for the unique electronic structure modulation induced by the high-entropy single-atom configuration. Notably, the in situ electron holography characterization (Figure 4f) clearly demonstrates that applied electric fields induce significant electron density redistribution on the catalyst surface, leading to enhanced charge heterogeneity and consequently a remarkable improvement in the adsorption and activation efficiency of reactive species such as H^+ [40]. Particularly, it is noteworthy that the incorporation of high-entropy single atoms endows the catalyst surface with exceptionally

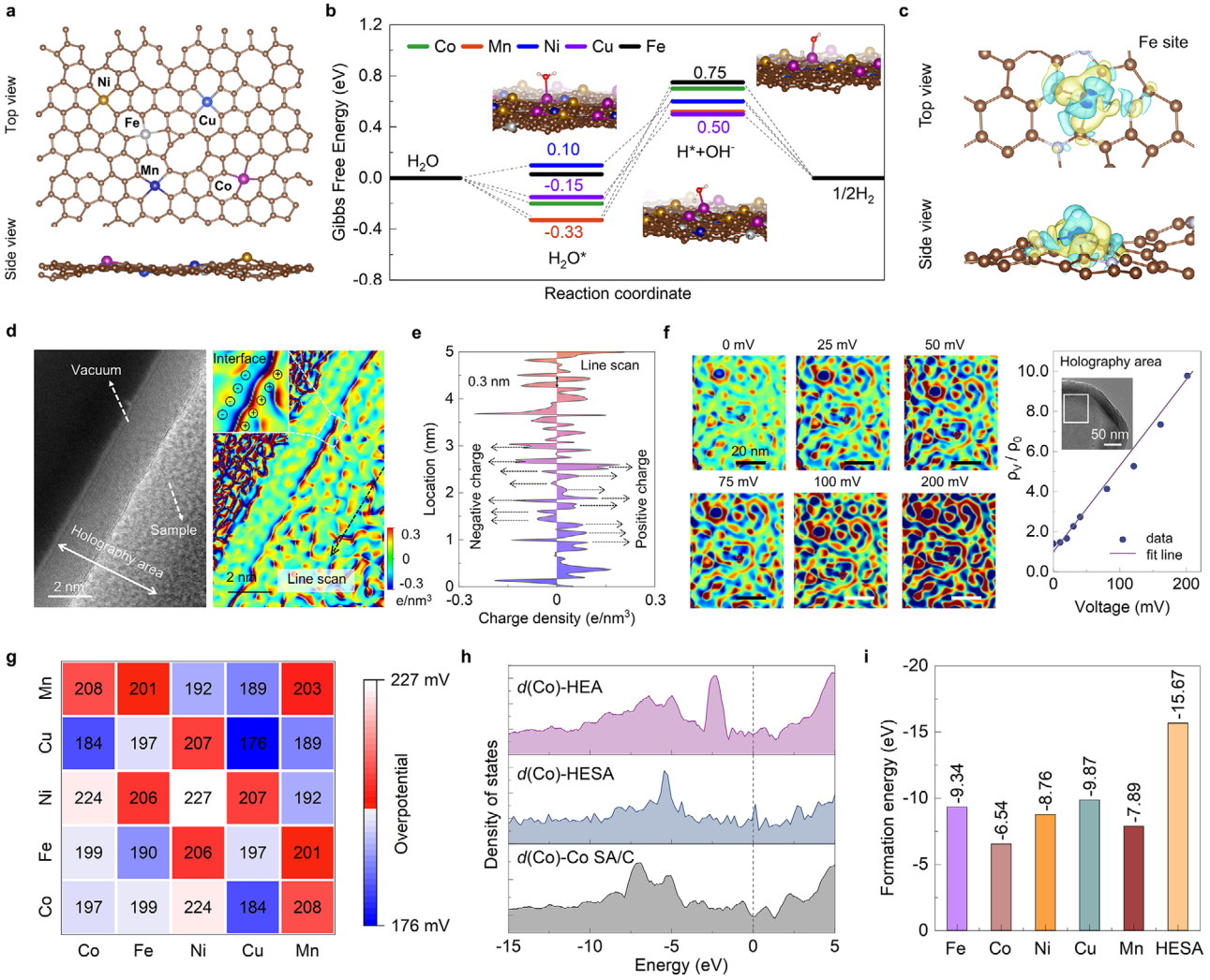

Figure 4 | Electronic structure analysis and the prediction of alkaline HER activity of HESA catalyst. (a) The computational modeling of HESA catalyst. (b) Reaction energy profile for water dissociation on various catalytic sites of HESA catalyst. (c) Top and side views of the differential charge density at the Fe site in HESA catalyst, where blue represents electron depletion and yellow represents electron accumulation. (d) Electron holography (left), charge density (right) for HESA catalyst surface and (e) the corresponding quantified charge density values as a function of distance along the black arrow profile. (f) In situ electron holography charge density under various enhanced voltages from 0 to 200 mV (left) and the quantified values as a function of voltage for HESA catalyst (right). (g) Heatmap illustrating the overpotential distribution of binary single-atom catalysts, where color (red to blue) intensity correlates with overpotential. (h) Projected density of states for HESA catalyst. (i) The formation energy of single atom for Fe, Co, Ni, Cu, Mn and HESA catalyst, respectively.

sensitive and linearly responsive characteristics to electric field stimulation.

Orthogonal LSV tests confirm the exceptional performance of HESA catalyst, surpassing binary or single-atom catalysts (Figure 4g; Figures S18 and S19), attributing to unique cooperative active sites that balance hydrolysis and desorption barriers while suppressing active site deactivation through entropy stabilization, providing crucial theoretical guidance for designing next-generation electrocatalysts. Co is used as an observation window to illustrate the modulation of local electronic states in the high-entropy single-atom system, while the contributions of the other metals are inherently reflected in the density of states (DOS). Band structure and DOS (Figure 4h; Figure S20) demonstrate appropriate *d*-band contributions near the Fermi level for Co site with the HESA catalyst. This d-electron interaction establishes a more stable electronic configuration and maintains appropriate adsorption strength for catalytic intermediates. Formation energy calculations (Figure 4i) reveal that the HESA system exhibits significantly lower formation energy (−15.67 eV) compared to single-component single-atom systems, primarily attributed to the increased configurational entropy from random distribution of multiple elements, which reduces the free energy of the system and provides a theoretical basis for the exceptional stability of the catalyst.

3 | Discussion

In summary, this work highlights the significance of designing multifunctional sites through single-atom engineering to enhance the reactivity of HER electrode surfaces under

alkaline conditions. Specifically, the design of discretely distributed multiple atomic species, combined with a highly stable carbon layer as a barrier, provides an optimized surface for water dissociation, overcoming the limitations of either overly strong or weak adsorption of key intermediates during the alkaline HER process. This approach also offers a novel perspective on improving HER performance by tailoring surface electronic structures through single-atom design. Furthermore, the HESA catalyst demonstrates significantly enhanced HER performance in alkaline media, characterized by an ultralow overpotential and exceptional stability. This study underscores the potential of structural modulation in regulating electrochemical interfaces to enhance electrocatalytic efficiency.

4 | Experimental Section

4.1 | Materials

Iron (II) acetate, cobalt (II) acetate tetrahydrate, nickel (II) acetate tetrahydrate, copper (II) acetate monohydrate, manganese (II) acetate, dopamine, trimethylol aminomethane hydrochloride, polyvinylpyrrolidone (K30, average molecular weight 40 000), ethanol and methanol were obtained from Aladdin. Water used in all the experiments was purified using a Milli-Q water purification system (Simplicity C9210). All chemicals were analytically pure reagents and were used without further purification.

4.2 | Synthesis of HESA Catalyst

The sample was synthesized with 0.25 mmol of iron (II) acetate, 0.25 mmol of cobalt (II) acetate tetrahydrate, 0.25 mmol of nickel (II) acetate tetrahydrate, 0.25 mmol of copper (II) acetate monohydrate, 0.25 mmol of manganese (II) acetate, and 1.5 g of polyvinylpyrrolidone dissolved in 80 mL of anhydrous ethanol. After stirring for 15 min, the above mixed solution was transferred to a 100 mL stainless steel autoclave with polytetrafluoroethylene liner and reacted at 90°C for 6 h, then cooled to room temperature naturally. The precipitation (the precursor of the catalyst) was collected by centrifugation, washed with ethanol 3 times, and dried in a vacuum environment. 100 mg of precursor was dispersed in methanol solution (100 mL) containing 30 mg of trimethylol aminomethane hydrochloride, ultrasonicated for 30 min, 50 mg dopamine hydrochloride was dispersed, and agitation was performed for 12 h and centrifugation, then stirred in H_2O (100 mL) for 2 h and centrifugation, dried in vacuum and calcined 350°C in nitrogen for 2 h.

4.3 | Synthesis of HEA Catalyst and Single-Atom Catalysts with Different Elements

The preparation method of HEA catalyst is similar to that of HESA catalyst, with the key distinctions being an increased calcination temperature of 600°C and the omission of the 2 h stirring step in water.

Additionally, binary single-atom catalysts (CoFe, CoNi, CoCu, CoMn, FeNi, FeCu, NiCu, NiMn and CuMn) were prepared using the same method as the HESA catalyst, but with equimolar amounts (0.625 mmol each) of the corresponding metal salts instead of the mixed metal precursors used for the HESA catalyst. Single-atom catalysts (Fe, Co, Ni, Cu, Mn SA catalysts) were prepared using the same method as the HESA catalyst, but with amounts (1.25 mmol each) of the corresponding metal salts instead of the mixed metal precursors used for HESA catalyst.

4.4 | Structural Characterization

The morphology and structure of the samples were analyzed using a Hitachi S-4800 field emission scanning electron microscope operated at 5 kV, a JEOL JEM-2100F transmission electron microscope (TEM) operated at 200 kV, and a dual spherical aberration-corrected TEM (FEI, Titan Themis Z, 300 kV). In situ multi-physics off-axis holography was performed using a modified TEM (JEOL, JEM-2100F, 200 kV) with applied current pulses varying from 0 to 100 mV. The crystalline phases of the products were characterized using an X-ray diffractometer (Bruker, D8-Advance) with Cu Kα radiation. The chemical compositions were determined using an inductively coupled plasma optical emission spectrometer (PerkinElmer, PE-8000). X-ray photoelectron spectroscopy (Kratos, AXIS Kratos Supra+, Al-Kα source) was conducted to analyze the surface chemical states and compositions of the samples, utilizing contaminant carbon (C 1*s*, ≈284.8 eV) as a reference. The extended X-ray absorption fine structure (EXAFS) was measured by a laboratory-based high-energy X-ray absorption spectroscope (Hp Spectroscopy GmbH) at the energy range of 5–12 keV. The ^{1}H magic angle spinning nuclear magnetic resonance experiments were performed on a Bruker AVANCE III 400 WB spectrometer at 400.47 MHz. Raman spectra were acquired using a confocal Raman microscope (LabRAM HR Evolution, Horiba Jobin Yvon). The excitation source was a 633 nm laser with a power of 17 mW.

4.5 | Electrochemical Measurements

All electrochemical measurements were performed with a CHI 760E electrochemical workstation in a standard three-electrode system using the prepared catalysts as the working electrode, a graphite rod as the counter electrode and an Hg/HgO electrode (in 1.0 M KOH) as the reference electrode. All measured potentials were referred to the reversible hydrogen electrode (RHE) using the following equation:

$$E\,(\mathrm{RHE}) = E\,(\mathrm{Hg/HgO}) + 0.059 \times \mathrm{pH} + 0.098 \quad (1)$$

with the current densities (j) normalized by geometric surface area. Electrochemical impedance spectroscopy was carried out from 100 kHz to 0.1 Hz at the given potential with AC amplitude of 10 mV. All polarization curves were 95% iR-corrected. The electrochemical cell was assembled by sequentially stacking the cathode plate, cathode, anion exchange membrane (2.5 × 2.5 cm^2), anode, and anode plate. Both compartments were fed with 1 M KOH. The working area of each electrode was 1 cm^2 with the tightening torque of 2 N. The cell featured serpentine flow channels and was operated between 1.0 and 2.5 V. The cathode and anode were both fabricated by drop-casting 200 μL ink onto 1 cm^2 carbon paper (Toray TGP-H-060) at 100°C to achieve a loading of 1 mg cm^{-2}.

Author's Contribution

H.H. and R.C. designed and supervised the experiments, as well as leading the manuscript writing. B.L., M.Y. and Y.L. contributed to material synthesis and performed various analyses, including electron microscopy, XRD, EELS and electronic holography analysis. J.Z. and Y.M. designed and performed experiments of HER experiment. X.X. and J.S. carried out DFT simulations. All authors participated in the results discussions and contributed to manuscript preparation.

Funding

This work was supported by the National Key Research Program of China (No. 2024YFA1408000, 2024YFA1208902, 2021YFA1200600, 2022YFA1503502), the National Natural Science Foundation of China (No. 52231007, 12327804, T2321003, 22088101, 22405050), the Science and Technology Commission of Shanghai Municipality (No. 24ZR1406400), and Key Laboratory of High Temperature Electromagnetic Materials and Structure of MOE (No. KB202401), Fund of Science and Technology on Surface Physics and Chemistry Laboratory (No. JCKYS2023120201), and Shanghai Municipal Education Commission (No. 24KXZNA06).

Conflicts of Interest

The authors declare no conflicts of interest.

Data Availability Statement

The data that support the findings of this study are available from the corresponding author upon reasonable request.

References

1. Q. Zhu, Y. Huang, D. Zhou, et al., "Automated Synthesis of Oxygen-Producing Catalysts from Martian Meteorites by a Robotic AI Chemist," *Nature Synthesis* 3 (2024): 319–328, https://doi.org/10.1038/s44160-023-00424-1.

2. L. Yang, Z. Ni, Y. Zhao, et al., *ACS Catal* 14 (2024): 3151, https://pubs.acs.org/doi/10.1021/acscatal.4c01829.

3. N. Daelman, M. Capdevila-Cortada, and N. López, "Dynamic Charge and Oxidation state of Pt/CeO2 Single-Atom Catalysts," *Nature Materials* 18 (2019): 1215–1221, https://doi.org/10.1038/s41563-019-0444-y.

4. V. Muravev, A. Parastaev, Y. van den Bosch, et al., "Size of Cerium Dioxide Support Nanocrystals Dictates Reactivity of Highly Dispersed Palladium Catalysts," *Science* 380 (2023): 1174–1179, https://doi.org/10.1126/science.adf9082.

5. Y. Wang, P. Ren, J. Hu, et al., "Electron Penetration Triggering Interface Activity of Pt-Graphene for CO Oxidation at Room Temperature, " *Nature Communications* 12 (2021), 5814, https://doi.org/10.1038/s41467-021-26089-y.

6. R. Subbaraman, D. Tripkovic, K. Chang, et al., "Trends in Activity for the Water Electrolyser Reactions on 3d M(Ni,Co,Fe,Mn) hydr(oxy)oxide Catalysts," *Nature Materials* 11 (2012): 550–557, https://doi.org/10.1038/nmat3313.

7. J. Liang, J. Liu, L. Guo, et al., "CO_2 Hydrogenation Over Fe-Co Bimetallic Catalysts with Tunable Selectivity Through a Graphene Fencing Approach," *Nature Communications* 15 (2024): 512, https://doi.org/10.1038/s41467-024-44763-9.

8. T. Sun, Z. Tang, W. Zang, et al., "Ferromagnetic Single-Atom Spin Catalyst for Boosting Water Splitting," *Nature Nanotechnology* 18 (2023): 763–771, https://doi.org/10.1038/s41565-023-01407-1.

9. Q. He, Y. Zhou, L. Mou, et al., "Iron-Doped Ruthenium. with a Good Interfacial Environment Achieving Superior Hydrogen Evolution Activity Under Alkaline Conditions," *Energy & Environmental Science* 18 (2025): 1984–1991, https://doi.org/10.1039/D4EE05356G.

10. Z. Pei, X. F. Lu, H. Zhang, Y. Li, D. Luan, and X. W. Lou, "Highly Efficient Electrocatalytic Oxygen Evolution Over Atomically Dispersed Synergistic Ni/Co Dual Sites," *Angewandte Chemie, International Edition* 134 (2022): 202207537, https://doi.org/10.1002/ange.202207537.

11. J. Chen, X. Gao, Y. Wu, et al., "Facile Synthesis of the TiO_2 -Supported Ultrathin Palladium Facet Composite Catalyst With Superior Metal Dispersion and Enhanced Catalytic Performance in Formic Acid Electro-Oxidation," *The Journal of Physical Chemistry C* 127 (2023): 22608–22617, https://doi.org/10.1021/acs.jpcc.3c05482.

12. A. Kumar, V. Q. Bui, J. Lee, et al., "Moving Beyond Bimetallic-Alloy to Single-Atom Dimer Atomic-Interface for all-pH Hydrogen Evolution," *Nature Communications* 12 (2021), 6766, https://doi.org/10.1038/s41467-021-27145-3.

13. C. Xia, Y. Qiu, Y. Xia, et al., "General Synthesis of Single-Atom Catalysts with High Metal Loading Using Graphene Quantum Dots," *Nature Chemistry* 13 (2021): 887–894, https://doi.org/10.1038/s41557-021-00734-x.

14. S. Tang, M. Xie, S. Yu, et al., "General Synthesis of High-Entropy Single-Atom Nanocages for Electrosynthesis of Ammonia From Nitrate," *Nature Communications* 15 (2024): 6932, https://doi.org/10.1038/s41467-024-51112-3.

15. S. H. Al-Hilfi, X. Jiang, J. Heuer, et al., "Single-Atom Catalysts Through Pressure-Controlled Metal Diffusion," *Journal of the American Chemical Society* 146 (2024): 19886–19895, https://doi.org/10.1021/jacs.4c03066.

16. Z. Chen, M. Yang, Y. Li, et al., "Termination-Acidity Tailoring of Molybdenum Carbides for Alkaline Hydrogen Evolution Reaction," *Nature Communications* 16 (2025): 418, https://doi.org/10.1038/s41467-025-55854-6.

17. H. Jiang, W. Yang, M. Xu, et al., "Single Atom Catalysts in Van Der Waals Gaps," *Nature Communications* 13 (2022): 6863, https://doi.org/10.1038/s41467-022-34572-3.

18. Y. Li, C. Peng, Y. Sun, et al., "Operando Elucidation of Hydrogen Production Mechanisms on Sub-Nanometric High-Entropy Metallenes," *Nature Communications* 15 (2024): 10222, https://doi.org/10.1038/s41467-024-54589-0.

19. S. Yu, H. Yamauchi, S. Wang, et al., "CO_2-to-Methanol Electroconversion on a Molecular Cobalt Catalyst Facilitated by Acidic Cations," *Nature Catalysis* 7 (2024): 1000–1009, https://doi.org/10.1038/s41929-024-01197-2.

20. J. Chen, X. Gao, Y. Wu, et al., "Facile Synthesis of the TiO_2-Supported Ultrathin Palladium Facet Composite Catalyst with Superior Metal Dispersion and Enhanced Catalytic Performance in Formic Acid Electro-Oxidation," *Journal of Physical Chemistry C* 127 (2023): 22608–22617, https://doi.org/10.1021/acs.jpcc.3c05482.

21. Q. Yao, H. Ding, L. Zhang, et al., "MAS NMR Studies on the Formation and Structure of Oxygen Vacancies on the CeO_2 {111} Surface Under Reducing Atmosphere," *Journal of Physical Chemistry C* 128 (2024): 9962–9972, https://doi.org/10.1021/acs.jpcc.4c01861.

22. Y. Liu, G. Chen, R. Ge, et al., "Construction of CoNiFe Trimetallic Carbonate Hydroxide Hierarchical Hollow Microflowers with Oxygen Vacancies for Electrocatalytic Water Oxidation," *Advanced Functional Materials* 32 (2022): 2201234, https://doi.org/10.1002/adfm.202200726.

23. Y. Tian, Z. Mao, L. Wang, and J. Liang, "Green Chemistry: Advanced Electrocatalysts and System Design for Ammonia Oxidation," *Small Structure* 4 (2023): 2200266, https://doi.org/10.1002/sstr.202200266.

24. P. Kiehl, M. Rohmer, and M. Bénard, "Electron Delocalization in Nickel Metallic Wires: A DFT Investigation of $Ni3(dpa)_4Cl_2$ and $[Ni_3(dpa)_4]^{3+}$ (dpa = Dipyridylamide) and Extension to Higher Nuclearity Chains," *Inorganic Chemistry* 43 (2004): 3151–3158, https://doi.org/10.1021/ic040011j.

25. M. Castro and D. R. Salahub, "Density-Functional Calculations for Small Iron Clusters: Fe*n*, Fe+ *n*, and Fe− *n* for n≤5," *Physical Review B* 49 (1994): 11842, https://doi.org/10.1103/PhysRevB.49.11842.

26. Q. Yao, H. Ding, L. Zhang, et al., "MAS NMR Studies on the Formation and Structure of Oxygen Vacancies on the CeO 2 {111} Surface Under Reducing Atmosphere," *The Journal of Physical Chemistry C* 128 (2024): 9962–9972, https://doi.org/10.1021/acs.jpcc.4c01861.

27. Q. Yao, L. Zhang, D. Huang, et al., "MAS NMR Studies on the Formation and Structure of Oxygen Vacancy on the CeO_2 {110} Surface Under a Reducing Atmosphere," *The Journal of Physical Chemistry C* 127 (2023): 13021–13033, https://doi.org/10.1021/acs.jpcc.3c02592.

28. W. Feng, M. Yu, L. Wang, et al., "Insights Into Bimetallic Oxide Synergy During Carbon Dioxide Hydrogenation to Methanol and Dimethyl Ether Over GaZrO x Oxide Catalysts," *ACS Catalysis* 11 (2021): 4704-4711, https://doi.org/10.1021/acscatal.0c05410.

29. Z. Yang, J. Yang, C. Yu, et al., "Rare-Earth Lanthanum Tailoring Mott–Schottky Heterojunction by Sulfur Vacancy Modification as a Bifunctional Electrocatalyst for Zinc–Air Battery," *Small Structures* 4 (2023): 2200267, https://doi.org/10.1002/sstr.202200267.

30. K. Zhang, L. Chen, and Z. Liu, "Do Rh-Hydride Phases Contribute to the Catalytic Activity of Rh Catalysts Under Reductive Conditions?," *Journal of the American Chemical Society* 146 (2024): 35416–35426, https://doi.org/10.1021/jacs.4c14404.

31. M. Li, F. Lin, S. Zhang, et al., "High-Entropy Alloy Electrocatalysts go to (Sub-)Nanoscale," *Science Advances* 10 (2024): eadn2877, https://doi.org/10.1126/sciadv.adn2877.

32. J. Shan, C. Ye, Y. Jiang, M. Jaroniec, Y. Zheng, and S. Qiao, "Metal-Metal Interactions in Correlated Single-Atom Catalysts," *Science Advances* 8 (2022): abo0762, https://doi.org/10.1126/sciadv.abo0762.

33. Y. Yao, Z. Huang, P. Xie, et al., "High Temperature Shockwave Stabilized Single Atoms," *Nature Nanotechnology* 14 (2019): 851–857, https://doi.org/10.1038/s41565-019-0518-7.

34. T. Pinheiro Araújo, C. Mondelli, M. Agrachev, et al., "Flame-made ternary Pd-$In2O_3$-ZrO_2 catalyst with Enhanced Oxygen Vacancy Generation for CO2 Hydrogenation to Methanol," *Nature Communications* 13 (2022): 5610, https://doi.org/10.1038/s41467-022-33391-w.

35. Q. Yao, H. Ding, L. Zhang, et al., "MAS NMR Studies on the Formation and Structure of Oxygen Vacancies on the CeO_2 {111} Surface Under Reducing Atmosphere," *The Journal of Physical Chemistry C* 128 (2024): 9962–9972, https://doi.org/10.1021/acs.jpcc.4c01861.

36. Q. Yao, L. Zhang, D. Huang, et al., "MAS NMR Studies on the Formation and Structure of Oxygen Vacancy on the CeO 2 {110} Surface Under a Reducing Atmosphere," *The Journal of Physical Chemistry C* 127 (2023): 13021–13033, https://doi.org/10.1021/acs.jpcc.3c02592.

37. W. Feng, M. Yu, L. Wang, et al., "Insights Into Bimetallic Oxide Synergy During Carbon Dioxide Hydrogenation to Methanol and Dimethyl Ether Over GaZrO x Oxide Catalysts," *ACS Catalysis* 11 (2021): 4704–4711, https://doi.org/10.1021/acscatal.0c05410.

38. Z. Yang, J. Yang, C. Yu, et al., "Rare-Earth Lanthanum Tailoring Mott–Schottky Heterojunction by Sulfur Vacancy Modification as a Bifunctional Electrocatalyst for Zinc–Air Battery," *Small Structures* 4 (2023): 2200267, https://doi.org/10.1002/sstr.202200267.

39. K. Zhang, L. Chen, and Z. Liu, "Do Rh-Hydride Phases Contribute to the Catalytic Activity of Rh Catalysts Under Reductive Conditions?," *Journal of the American Chemical Society* 146 (2024): 35416–35426, https://doi.org/10.1021/jacs.4c14404.

40. P. Kumari, S. K. Mohapatra, P. Yadav, R. J. Choudhary, A. Lakhani, and R. R. Shahi, "Integrative Approach to Enhance the Soft Magnetic Properties of Co35Cr5Fe10Ni30Ti20-xAlx (x= 10, 15, 20) High Entropy Alloys," *Journal of Alloys and Compounds* 1005 (2024): 175890, https://doi.org/10.1016/j.jallcom.2024.175890.

Supporting Information

Additional supporting information can be found online in the Supporting Information section.

Supporting file: aenm70455-sup-0001-SuppMat.docx